ScienceAdvances
AAAS

advances.sciencemag.org/cgi/content/full/3/1/e1601814/DC1

Supplementary Materials for

Single-shot real-time video recording of a photonic Mach cone induced by a scattered light pulse

Jinyang Liang, Cheng Ma, Liren Zhu, Yujia Chen, Liang Gao, Lihong V. Wang

Published 20 January 2017, *Sci. Adv.* **3**, e1601814 (2017)
DOI: 10.1126/sciadv.1601814

The PDF file includes:

Other Supplementary Material for this manuscript includes the following:
(available at advances.sciencemag.org/cgi/content/full/3/1/e1601814/DC1)

- movie S1 (.mov format). Simulated instantaneous light-scattering pattern in a thin scattering sheet under superluminal conditions (M_p = 1.4).
- movie S2 (.mov format). Simulated instantaneous light-scattering pattern in a thin scattering sheet under subluminal conditions (M_p = 0.8).
- movie S3 (.mov format). Animated illustration of the LLE-CUP system.
- movie S4 (.mov format). Experimentally imaged laser pulse propagation under superluminal conditions (M_p = 1.4) through a thin scattering plate assembly that

contains air (refractive index $n_s = 1.0$) as the source tunnel medium and silicone rubber (refractive index $n_d = 1.4$) mixed with scattering aluminum oxide powder as the medium of the display panels.

- movie S5 (.mov format). Experimentally imaged laser pulse propagation under subluminal conditions ($M_p = 0.8$) through a thin scattering plate assembly that contains liquid oil with a high refractive index (refractive index $n_s = 1.8$) as the source tunnel medium and silicone rubber (refractive index $n_d = 1.4$) mixed with scattering aluminum oxide powder as the medium of the display panels.
- movie S6 (.mov format). Comparative image reconstructions of a superluminal light wavefront sweeping across a car-model target using first-generation CUP and LLE-CUP.

section S1. Simulation of a photonic Mach cone.

Analytical model

We discuss the mathematical formulation of a photonic Mach cone in this Subsection. Figure S1 shows the Cartesian coordinates used to analyze the phenomenon. The source is located at $\mathbf{r_s}$, labeled by (x_s, y_s, z_s), and the observation is made at $\mathbf{r}$, labeled by (x, y, z). We denote $\mathbf{R} = \mathbf{r} - \mathbf{r_s}$ as the vector pointing from the source to the observation point.

The incident laser pulse experiences light scattering in an elementary volume dV', located at $\mathbf{r_s}$. The excited scatterers have a number density N, an average radius a, and a refractive index n_sc. The wave number of the incident beam is k. If $ka \ll 1$, the scattering can be treated in the context of Rayleigh scattering. The $z = 0$ plane was chosen to display the instantaneous light scattering pattern. In our experiment, light was polarized along the z axis. This condition eliminated the angular dependence of the scattered light distribution on the $z = 0$ plane. Moreover, the electric fields originating from randomly distributed scatterers are considered to be uncorrelated due to the random and variable (>2π on average) phase delays from the scatterers to the observation point; consequently, fully developed speckles are formed. For macroscopic observation, because the effective pixel of the detector at the object plane usually has a size in millimeters, the observed light pattern can be modeled with an intensity distribution ensemble-averaged over speckle grains. Therefore, we calculate the final light distribution by adding the intensity values from the scatterers (*57*). The expected light intensity contributed by the elementary volume dV' can be expressed as (*58*)

$$dI = \frac{k^4 a^6}{|\mathbf{R}|^2} \Delta_\mathrm{n}^2 I_0 N dV' \tag{S1}$$

where I_0 is the incident light intensity and $\Delta_\mathrm{n} = (n_\mathrm{sc}^2 - n_\mathrm{s}^2)/(n_\mathrm{sc}^2 + 2n_\mathrm{s}^2)$. We assume that the incident light pulse has a Gaussian intensity distribution along the x, y, and z axes and travels along the $+x$ direction at a speed c_s, which exceeds the speed in the display panels, c_d. The total light intensity at $\mathbf{r}$ is therefore

$$I(\mathbf{r},t) = k^4 a^6 \Delta_\mathrm{n}^2 I_0 N \iiint \frac{1}{|\mathbf{R}|^2} \exp\left[-\frac{y_\mathrm{s}^2}{2\sigma_y^2} - \frac{z_\mathrm{s}^2}{2\sigma_z^2} - \frac{\left(x_\mathrm{s} + \frac{c_\mathrm{s}}{c_\mathrm{d}}|\mathbf{R}| - c_\mathrm{s} t\right)^2}{2\sigma_x^2} \right] dx_\mathrm{s} dy_\mathrm{s} dz_\mathrm{s} \tag{S2}$$

In eq. S2, σ_i ($i = x, y, z$) denotes the pulse width along direction i, the term $-c_s t$ implies travelling along the $+x$ direction, and $c_\mathrm{s}|\mathbf{R}|/c_\mathrm{d}$ accounts for the retarded response at the observation point. The magnitude of $\mathbf{R}$ can be calculated from $|\mathbf{R}| = \sqrt{(x - x_\mathrm{s})^2 + (y - y_\mathrm{s})^2 + (z - z_\mathrm{s})^2}$, and is hereafter denoted by a real number R.

Equation S2 can be rewritten in a time-convolution form as

$$I(\mathbf{r},t) = k^4 a^6 \Delta_\mathrm{n}^2 I_0 N \iiint dx_\mathrm{s} dy_\mathrm{s} dz_\mathrm{s} \int d\tau \frac{\delta\left(t - \tau - \frac{R}{c_\mathrm{d}}\right)}{R^2} \exp\left[-\frac{y_\mathrm{s}^2}{2\sigma_y^2} - \frac{z_\mathrm{s}^2}{2\sigma_z^2} - \frac{(x_\mathrm{s} - c_\mathrm{s}\tau)^2}{2\sigma_x^2} \right] \tag{S3}$$

where $\delta(\cdot)$ is the Dirac delta function. We then proceed with the following variable substitution

$$\Delta y = y - y_\mathrm{s}, \Delta z = z - z_\mathrm{s}, \text{and } \Delta x = x - x_\mathrm{s} + c_\mathrm{s}\tau \tag{S4}$$

to reach a spatial convolution form

$$I(\mathbf{r},t) = k^4 a^6 \Delta_\mathrm{n}^2 I_0 N \iiint d\Delta x d\Delta y d\Delta z \left[\int d\tau \frac{\delta\left(t-\tau-\frac{R}{c_\mathrm{s}}\right)}{R^2}\right] \exp\left\{-\left[\frac{(x-\Delta x)^2}{2\sigma_x^2} + \frac{(y-\Delta y)^2}{2\sigma_y^2} + \frac{(z-\Delta z)^2}{2\sigma_z^2}\right]\right\} \tag{S5}$$

The time integration over τ in the bracket on the right-hand side of eq. S5 can be interpreted as a temporal impulse response of the system, and it yields a closed-form solution by setting $\Delta\rho^2 = \Delta y^2 + \Delta z^2$

$$J(\Delta x, \Delta y, \Delta z, t) = \int \frac{\delta\left(t-\tau-\frac{\sqrt{\Delta\rho^2+(\Delta x - c_\mathrm{s}\tau)^2}}{c_\mathrm{d}}\right)}{\Delta\rho^2+(\Delta x - c_\mathrm{s}\tau)^2} d\tau \tag{S6}$$

Equation S6 can be evaluated by

$$J = \sum_{i=1}^{2} \frac{f(\tau_i)}{|g'(\tau_i)|} \tag{S7}$$

where

$$f(\tau) = \frac{1}{\Delta\rho^2+(\Delta x - c_\mathrm{s}\tau)^2} \tag{S8}$$

$$g(\tau) = t - \tau - \frac{\sqrt{\Delta\rho^2+(\Delta x - c_\mathrm{s}\tau)^2}}{c_\mathrm{d}} \tag{S9}$$

$$g'(\tau) = -1 - \frac{c_\mathrm{s}^2\tau - c_\mathrm{s}x}{c_\mathrm{d}\sqrt{\Delta\rho^2+(\Delta x - c_\mathrm{s}\tau)^2}} \tag{S10}$$

and τ_i are the solutions of $g(\tau) = 0$, which are found to be

$$\tau_{1,2} = \frac{1}{B_0^2}\left(\frac{xc_\mathrm{s}}{c_\mathrm{d}} - t \pm \frac{\sqrt{Y}}{c_\mathrm{d}}\right) \tag{S11}$$

In eq. S11

$$Y = q^2 - B_0^2\Delta\rho^2 \tag{S12}$$

where

$$q = c_\mathrm{s}t - \Delta x \text{ , and} \tag{S13}$$

$$B_0 = \sqrt{\frac{c_s^2 - c_d^2}{c_d^2}} \tag{S14}$$

is the Prandtl-Glauert coefficient.

It should be noted that according to eq. S6, the location of the excitation impulse is $\Delta x(t) = c_s t$ at the time point t, so both solutions τ_i $(i = 1, 2)$ should satisfy

$$\tau_i \leq t \text{ for } z \leq c_s t \tag{S15}$$

which can be verified by simple algebra.

Setting eq. S9 to zero, we get the relationship

$$c_d(t - \tau_i) = \sqrt{\Delta\rho^2 + (\Delta x - c_s\tau_i)^2} \tag{S16}$$

by inserting eqs. S8, S10, S11, and S16 into eq. S7. After mathematical manipulations, we get the closed-form solution for the impulse response, expressed as

$$J = \frac{c_s}{c_d}\frac{2q}{(q^2 + \Delta\rho^2)\sqrt{Y}} \tag{S17}$$

Equation S17 describes the shape of the instantaneous light scattering pattern, which is depicted as a photonic Mach cone for $M_p > 1$. The cone boundary is defined by setting $Y = 0$. Inserting eq. S12, we can easily verify the cone angle (Eq. 1 in the Main Text). On the cone boundary, the impulse response intensity theoretically goes to infinity (eq. S17). In fig. S2, A, the impulse response for a photonic Mach number of $M_p = 1.4$ is plotted. For display purposes, large values near the cone boundary are saturated to 5 mm^{-2}.

By inserting eq. S17 into eq. S5 (Eq. 3 in the Main Text) and numerically evaluating the volumetric integral, we find the exact expected intensity distribution of the cone. Figure S2, B depicts the intensity distribution of a cone excited by a Gaussian pulse in the $z = 0$ plane. In the simulation, we assumed $M_p = 1.4$ and the intensity full-width at half-maximum (FWHM) of the pulse to be 1 mm in both x and y directions.

Monte Carlo simulation

The theoretical model described in the preceding Subsection deals with a fully-developed cone. In our experiment, however, the sample has a finite length; therefore, the cone undergoes a build-up process before reaching its steady state. To account for this dynamic process, we simulated the experimentally investigated superluminal condition ($M_p = 1.4$) and subluminal condition ($M_p = 0.8$) using the time-resolved Monte Carlo method.

To reduce computational complexity, we assumed a thin scattering sheet with negligible thickness to perform the simulation in 2D. Having a uniform scattering coefficient, this scattering sheet had dimensions of 37.5 mm × 50 mm. Light excitation was introduced from left to right along the central line of the sheet. An infinitely narrow beam entered the left edge of the sheet, traveled along the $+x$ direction with a speed of c_s, and encountered a sequence of scattering events during its propagation. The location of each scattering event was randomly determined, with a uniform

probability density distribution along the x axis. Each scattering event emitted an outgoing spherical wave, which subsequently deposited photons with energy $1/R^2$ to those voxels $R = c_{\mathrm{d}}(t - t_{\mathrm{s}})$ away from the scatterer, with t_{s} being the instant of that particular scattering event. The above scattering process was repeated as *t* progressed, and all voxels kept accumulating photons according to the procedure above until the beam left the right edge of the sheet. A total of 10^5 scattering events were used in each simulation. At last, the result was convolved with a Gaussian probability density function in 2D (i.e., x and y axes) to simulate excitation by a spatiotemporally finite pulse. The numerical results, shown in Fig. 2 in the Main Text (with corresponding movies in movies S1 and S2), are consistent with the experimental results.

section S2. Forward model of LLE-CUP.

Overview

For a dynamic scene with an intensity distribution of $I(x, y, t)$, LLE-CUP generates three projection views: a time-unsheared view, and two time-sheared views with complementary encoding (fig. S3). For simplicity of notation here, we make the following four assumptions. First, the imaging system has a unit magnification. Second, the dynamic scene can be perfectly imaged to the digital micromirror device (DMD). Third, the external CCD camera and the internal CCD camera of the streak camera have the same pixel size, denoted as d. Fourth, we only explicitly express the time delay due to the streak camera.

The time-unsheared view

In the time-unsheared view, the input scene is spatially low-pass filtered by the external CCD's camera lens (Fig. 3 in the Main Text). The intensity distribution on the external CCD camera, $I_{F0}(x'_u, y'_u, t)$, is given by

$$I_{F0}(x'_u, y'_u, t) = \boldsymbol{F_0}\{I(x, y, t)\} \tag{S18}$$

where the subscript u stands for "unsheared", $\boldsymbol{F_0}$ denotes the spatial low-pass filtering operator in the time-unsheared view. With the spatiotemporal integration operator $\boldsymbol{T}$, the optical energy measured by the $[m, n]$ pixel on the CCD camera is given by

$$\begin{aligned} E_0[m, n] &= \boldsymbol{T}\{I_{F0}(x'_u, y'_u, t)\} \\ &= \int dx'_u \int dy'_u \left\{ \left[\int dt\, I_{F0}(x'_u, y'_u, t) \right] \cdot \mathrm{rect}\left[\frac{x'_u}{d} - \left(m + \frac{1}{2}\right), \frac{y'_u}{d} - \left(n + \frac{1}{2}\right) \right] \right\} \end{aligned} \tag{S19}$$

which is essentially a Radon transform measurement from one angle (fig. S4, A).

Complementary time-sheared views

In addition to the time-unsheared view, two complementary time-sheared views are acquired. For the first time-sheared view, the intensity distribution of the dynamic scene is first spatially encoded by a pseudo-random binary pattern displayed on the DMD, $c_1(x, y)$, yielding the following intensity distribution

$$I_{C1}(x, y, t) = c_1(x, y) I(x, y, t) \tag{S20}$$

Then, the spatially encoded dynamic scene passes through the imaging system to the entrance port of the streak camera. It is spatially low-pass filtered by the 4*f* imaging system between the DMD and the streak camera

$$I_{F1}(x, y, t) = \boldsymbol{F_1}\{I_{C1}(x, y, t)\} \tag{S21}$$

where $\boldsymbol{F_1}$ denotes the spatial low-pass filtering operator in the first time-sheared view. Then, an image distortion operator is applied to $I_{F1}(x, y, t)$

$$I_{D1}(x, y, t) = \boldsymbol{D_1}\{I_{F1}(x, y, t)\} \tag{S22}$$

where $\boldsymbol{D_1}$ is due to image distortion from primarily the encoding arm and secondarily system misalignment.

Next, the dynamic scene is captured by the streak camera. The operation of the streak camera introduces a time delay, denoted as τ_{sc}. Here, we define the new time axis $t' = t + \tau_{\mathrm{sc}}$. Physically, t represents the arrival times of photons at the entrance of the streak camera, whereas t' denotes the arrival times of the photoelectrons at the phosphor screen. We also define the new spatial axes $x' = x$ and $y' = y - vt$, where v denotes the shearing velocity of the streak camera. Under this coordinate system, the temporal shearing along the vertical spatial axis can be expressed by

$$\begin{aligned} I_{S1}(x', y', t') &= \boldsymbol{S}\{I_{D1}(x, y, t)\} \\ &= I_{D1}(x', y' + v(t' - \tau_{\mathrm{sc}}), t' - \tau_{\mathrm{sc}}) \end{aligned} \tag{S23}$$

Here, the scaling factor to the intensity due to the shearing operation is neglected for simplicity.

Finally, $I_{S1}(x', y', t')$ is imaged by an internal CCD camera in the streak camera. Akin to the time-unsheared view, the optical energy measured by the $[m, n]$ pixel on the CCD takes the form of

$$\begin{aligned} E_1[m, n] &= \boldsymbol{T}\{I_{S1}(x', y', t')\} \\ &= \int dx' \int dy' \left\{ \left[\int dt'\, I_{S1}(x', y', t') \right] \cdot \mathrm{rect}\left[\frac{x'}{d} - \left(m + \frac{1}{2}\right), \frac{y'}{d} - \left(n + \frac{1}{2}\right) \right] \right\} \end{aligned} \tag{S24}$$

Similar to the first time-sheared view, the data acquisition process of the second time-sheared view is mathematically equivalent to successively applying a series of linear operators to the intensity distribution of the input dynamic scene (Eq. 5 in Materials and Methods). Specifically, the spatial encoding operator $\boldsymbol{C_2}$ is implemented by the encoding mask $c_2(x, y)$, which is complementary to that in the first time-sheared view (that is, $c_1(x, y) + c_2(x, y) = 1$). The operator $\boldsymbol{D_2}$ denotes the distortion for the second time-sheared view. The two time-sheared views in combination can be regarded as a Radon transform measurement from another angle (fig. S4, C and E). Altogether, LLE-CUP records two lossless projection views of the dynamic scene (fig. S4, F).

Discrete forward model

Equations in the above Subsection describe a continuous-to-discrete forward model for the LLE-CUP system. However, to use this forward model in a compressed sensing-based reconstruction algorithm, we need to further discretize the dynamic scene to derive a discrete-to-discrete model. To accommodate the streak camera's setting and simplify the notation, we choose a voxel of (d, d, τ_s) in size, in the *x*-*y*-*t* space, where $\tau_s = d/v$. Thus, the discrete form of the dynamic scene can be expressed as

$$\begin{aligned} I[m, n, k] = \int dt \int dx \int dy\, I(x, y, t) \\ \cdot \mathrm{rect}\left[\frac{x}{d} - \left(m + \frac{1}{2}\right), \frac{y}{d} - \left(n + \frac{1}{2}\right), \frac{t}{\tau_s} - \left(k + \frac{1}{2}\right) \right] \end{aligned} \tag{S25}$$

For readability, we use the same symbol, I, but a different indexing notation—square brackets—to denote the corresponding discrete form of the dynamic scene's intensity distribution.

The measurement of the time-unsheared view in eq. S19 can now be approximated by the following discrete form

$$E_0[m,n] = \frac{d^3}{v}\sum_k (h_0 * I)[m,n,k] \tag{S26}$$

where h_0 is the discrete convolution kernel of the operator $\boldsymbol{F}_0$, and $*$ denotes the 2D spatial convolution operation.

For the first time-sheared view, with the encoding mask discretized similarly to eq. S25, denoted as $c[m,n]$, we can express the discrete form of the encoded dynamic scene as

$$I_{C1}[m,n,k] = c_1[m,n] \cdot I[m,n,k] \tag{S27}$$

Therefore, eq. S24, representing the imaging model of the first time-sheared view, can be rewritten in a discrete form as

$$E_1[m,n] = \frac{d^3}{v}\sum_k (h_1 * I_{C1})[f_{D1}, g_{D1} + k, k] \tag{S28}$$

Here h_1 is the discrete convolution kernel of the operator $\boldsymbol{F}_1$, while f_{R1} and g_{R1} are the discrete coordinates transformed according to the operator $\boldsymbol{D}_1$. Given the calibrated 2D projective transformation (*68-70*) defined by a 3-by-3 matrix

$$\begin{bmatrix} h_{11} & h_{12} & h_{13} \\ h_{21} & h_{22} & h_{23} \\ h_{33} & h_{32} & 1 \end{bmatrix} \tag{S29}$$

the coordinates $f_{R1}$and g_{R1} can be explicitly expressed as

$$f_{D1} = \text{round}\left(\frac{h_{11}m + h_{12}n + h_{13}}{h_{31}m + h_{32}n + 1}\right) \tag{S30.1}$$

$$g_{D1} = \text{round}\left(\frac{h_{21}m + h_{22}n + h_{23}}{h_{31}m + h_{32}n + 1}\right) \tag{S30.2}$$

where $\text{round}(\cdot)$ gives the closest integer of the input real number. Following the same procedure, the discrete form of $E_2[m,n]$ can also be derived.

section S3. Image reconstruction of LLE-CUP.

To correct image distortions in the two time-sheared views using operators $\boldsymbol{D}_1$ and $\boldsymbol{D}_2$, we imaged a resolution target. No sweep voltage was applied to the streak camera. The external CCD camera directly imaged the resolution target. The DMD was controlled to set all micromirrors to be either "on" or "off" to direct the reflected light into two time-sheared views to image the resolution target. To compute the distortion operators, $\boldsymbol{D_1}$ and $\boldsymbol{D_2}$, an image intensity-based co-registration algorithm, using the 2D projective transformation model and the mean square error metric, was applied to the two time-sheared views.

Operator $\boldsymbol{D}_i$ $(i = 1, 2)$ is coupled with the shearing and spatiotemporal integration operators and has to be treated as part of the overall operator of the time-sheared views, $\boldsymbol{O_i} = \boldsymbol{TSD_iF_iC_i}$. To implement an iterative reconstruction method, an adjoint operator is required, which can be derived as $\boldsymbol{O}_i^* = \boldsymbol{C}_i^*\boldsymbol{F}_i^*\boldsymbol{D}_i^*(\boldsymbol{TS})^*$. The adjoint operators $\boldsymbol{C}_i^*$ and $(\boldsymbol{TS})^*$ have been discussed in our previous work (*54*). Since $\boldsymbol{D_i}$ is a discrete-to-discrete linear operator, its adjoint operator, $\boldsymbol{D}_i^*$, can be expressed as

$$\boldsymbol{D}_i^* I = \sum_{p=0}^{N_p-1} < \boldsymbol{D}_i e_p, I > e_p \tag{S31}$$

where $N_p = N_x \times N_y \times N_t$ is the total number of voxels in the entire datacube; e_p is the p-th basis of the datacube space, where only the p-th voxel is set to 1; and $<\cdot,\cdot>$ denotes the inner product operation. Since operator $\boldsymbol{D}_i$ is a point-to-point mapping in the image space, and e_p is a single-point image, the operation $< \boldsymbol{D}_i e_p, I > e_p$ is equivalent to picking the value of the mapped pixel in the input image I and putting it in the p-th pixel. To implement $\boldsymbol{D}_i^*$, we cached the results of $\boldsymbol{D}_i e_p$ in a point-to-point map and inversely mapped the input image pixel values to the corresponding output pixel.

In addition, the images of the resolution target captured in the three views were used to calculate the spatial low-pass filtering operator $\boldsymbol{F_j}$ $(j = 0, 1, 2)$. For each view, the line spread functions (LSFs) in both the horizontal and vertical axes in the bar group were analyzed. The averaged FWHM of the LSFs was used for the presumed Gaussian-shaped point spread function (PSF), which is used as the convolution kernel function of $\boldsymbol{F_j}$. In addition, because $\boldsymbol{F_j}$ accounts for spatial low-pass filtering of the optical system and is a convolution operation, the corresponding adjoint operator is a correlation operation with the same PSF. Since the Gaussian-shaped PSF is a real and spatially symmetric function, correlation and convolution are identical, i.e., $\boldsymbol{F}_j^* = \boldsymbol{F}_j$.

To find the linear operators $\boldsymbol{C_i}$ $(i = 1, 2)$ for the two time-sheared views, a uniform-intensity scene was used as the input image. Here, we first use the first time-sheared view as an example to illustrate the procedure. The encoding pattern displayed on the DMD was directly imaged onto the streak camera operated with zero shearing. In addition, a background image was acquired by setting all DMD pixels to "on" for the first time-sheared view. The image of the encoding pattern was divided by the background image to correct for the intensity non-uniformity pixel by pixel. Finally, the image of the intensity-corrected encoding pattern was deconvolved with $\boldsymbol{F_1}$ to calculate $\boldsymbol{C_1}$. For the second time-sheared view, the encoding pattern displayed on the DMD formed a complementary mask to the first time-sheared view. In addition, another background image was acquired by setting all DMD pixels to "off" for the second time-sheared view. Following the same procedure as described above, $\boldsymbol{C_2}$ can be obtained.

With the prior knowledge of $\boldsymbol{O}$, $I(x, y, t)$ can be estimated from the measurements from the three views, E, by solving the inverse problem of Eq. 6 in Materials and Methods. Because of the sparsity in the input scene, the image reconstruction can be realized by solving the following optimization problem

$$\hat{I} = \arg\min_{I} \left[\frac{1}{2} \|E - \boldsymbol{O}I\|^2 + \beta \Phi(I) \right] \tag{S32}$$

where the first term $\frac{1}{2}\|E - \boldsymbol{O}I\|^2$ represents the measurement fidelity and the regularization term $\Phi(I)$ encourages sparsity. The regularization parameter β adjusts the weight ratio between fidelity and sparsity. For LLE-CUP image reconstruction, a compressed-sensing reconstruction algorithm developed from two-step iterative shrinkage/thresholding (TwIST) algorithm (*60*) was employed. The three-dimensional total variation (TV) was chosen as the regularizer, given by

$$\begin{aligned} \Phi(I) = & \sum_{m} \sum_{n,k} \sqrt{\left(I_{m,n+1,k} - I_{m,n,k}\right)^2 + \left(I_{m,n,k+1} - I_{m,n,k}\right)^2} \\ & + \sum_{n} \sum_{m,k} \sqrt{\left(I_{m+1,n,k} - I_{m,n,k}\right)^2 + \left(I_{m,n,k+1} - I_{m,n,k}\right)^2} \\ & + \sum_{k} \sum_{m,n} \sqrt{\left(I_{m+1,n,k} - I_{m,n,k}\right)^2 + \left(I_{m,n+1,k} - I_{m,n,k}\right)^2} \end{aligned} \tag{S33}$$

section S4. Sample preparation.

The scattering plate assembly, containing the central source tunnel sandwiched by two display panels, was built in three steps. First, we used standard microscope cover slides to make two empty display panels with dimensions of 75 mm × 25 mm × 4 mm (fig. S6, A). Second, we mixed 50 mg of aluminum oxide (Al_2O_3) powder (Sigma-Aldrich, 265497) as light scatterers into 20 mL of liquid silicone rubber (Wacker Silicone, Elastosil RT 601A, refractive index 1.4). After complete mixing, we added rubber solidifier (Wacker Silicone, Elastosil RT 601B) and poured the mixture into the two empty display panels. For the top panel, the Al_2O_3-rubber scattering material filled the entire panel cavity (fig. S6, B). For the bottom panel, a 4-mm-deep space was left at the top (fig. S6, C) as the source tunnel. Both panels were left to solidify for 24 hours. Finally, we used two different materials for the source tunnel: (i) air with dry ice fog for the superluminal condition and (ii) high-refractive-index liquid oil (Ade Advanced Optics, refractive index 1.8) for the subluminal condition. The top panel was stacked above the bottom panel. The completed plate assembly is shown in fig. S6, D.

Supplementary figures

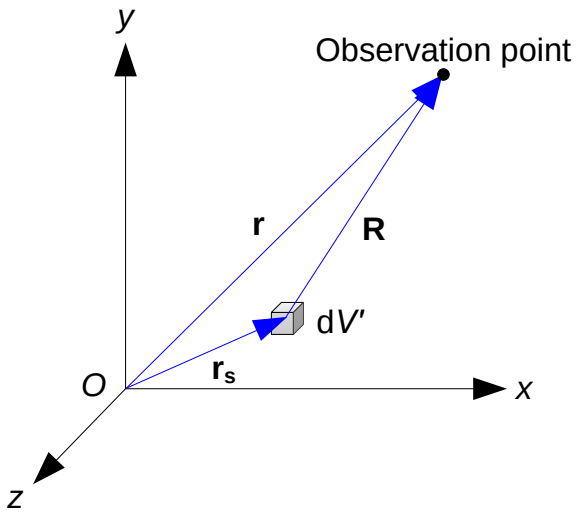

fig. S1. Cartesian coordinates used for analyzing the light-scattering dynamics.

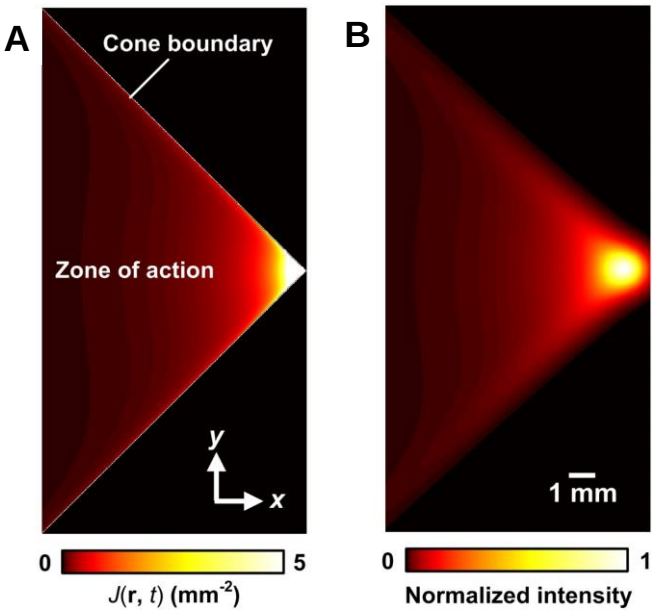

fig. S2. Numerical simulation of light-scattering dynamics in a thin scattering sheet. (**A**) Impulse response $J(\mathbf{r}, t)$ with $M_\mathrm{p} = 1.4$. (**B**) Normalized light intensity distribution of a cone excited by a Gaussian pulse with $M_\mathrm{p} = 1.4$. The Gaussian beam has an intensity full width at half maximum of 1 mm in both the x and y directions.

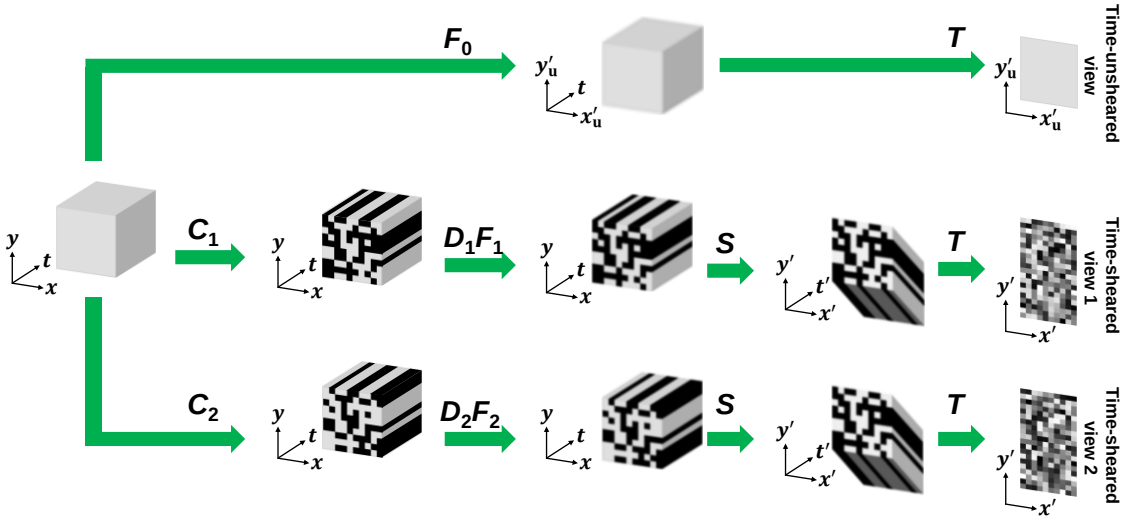

fig. S3. Schematic of the LLE-CUP data acquisition. t, t', time; x, y, spatial coordinates of the scene; x'_{u}, y'_{u}, spatial coordinates at the external CCD camera; x', y'spatial coordinates at the streak camera; $\boldsymbol{C_i}(i = 1, 2)$, spatial encoding operators; $\boldsymbol{F_j}(j = 0, 1, 2)$, spatial low-pass filtering operators, which blur the images as indicated in the figure; $\boldsymbol{D_i}$ $(i = 1, 2)$, image distortion operators; $\boldsymbol{S}$, temporal shearing operator; $\boldsymbol{T}$, spatiotemporal integration operator.

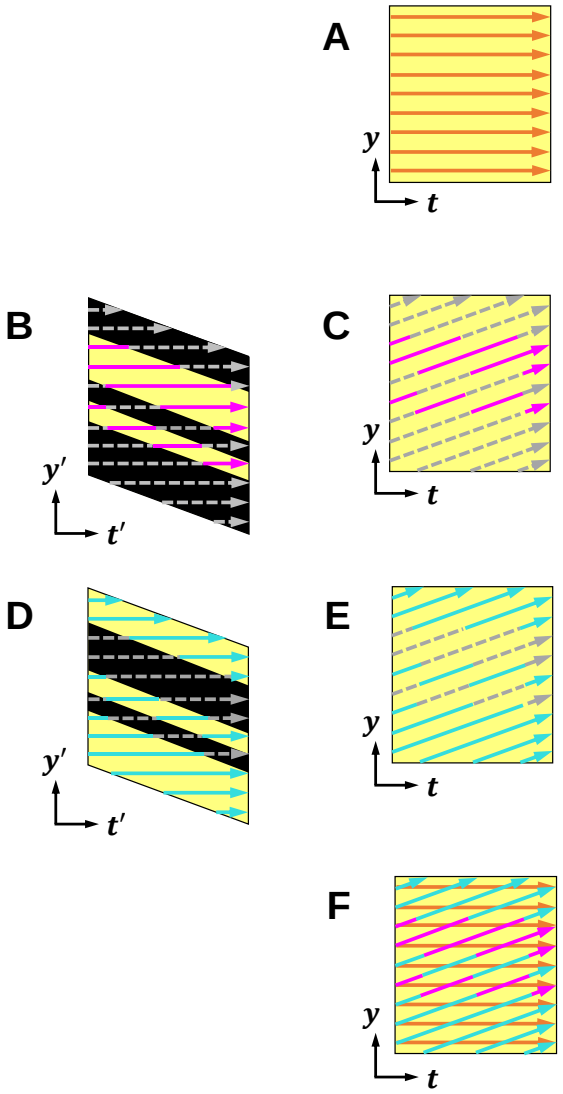

fig. S4. Illustration of multiview projections in LLE-CUP's data acquisition. The vertical spatial axis of the dynamic scene and that of the measurement are denoted by y and y', respectively. (**A**) Data acquisition in the time-unsheared view illustrated using a y-t cross section of the input scene. The direction of temporal integration is shown as the solid orange arrow. (**B**) Data acquisition in the first time-sheared view. Black areas in the y'-t' cross section show the blocked space due to the spatial encoding. The temporal integration operates in the direction indicated by the arrow. The preserved spatiotemporal information is marked by the solid magenta lines, whereas the lost spatiotemporal information is marked as the gray dashed lines. (**C**) Data acquisition in the first time-sheared view in the y-t coordinates. The temporal integration is along the tilted direction. (**D**) As (B), but showing the second time-sheared view. The preserved spatiotemporal information is marked by the turquoise solid lines. (**E**) As (C), but showing the second time-sheared view. (**F**) Data acquisition in LLE-CUP. The three-view projection implementation provides two lossless projection angles to the dynamic scene, where the complementary spatial encoding prevents spatiotemporal information loss.

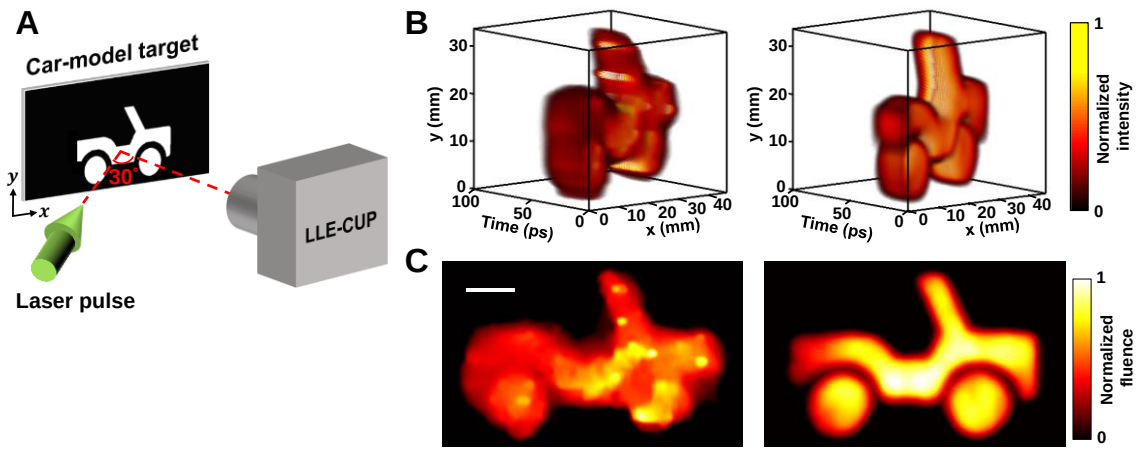

fig. S5. Characterization of image reconstruction in LLE-CUP. (**A**) Experimental setup for testing the LLE-CUP system. A collimated laser beam illuminates a car-model target obliquely. The LLE-CUP system is placed perpendicular to the target to collect the scattered photons. (**B**) Reconstructed x, y, t images representing the superluminal sweeping of a laser pulse's wavefront upon the car-model target, using first generation and LLE-CUP. (**C**) As (B) but showing the projected car-model target images by summing over the x, y, t datacube voxels along the t axis. Scale bar: 10 mm.

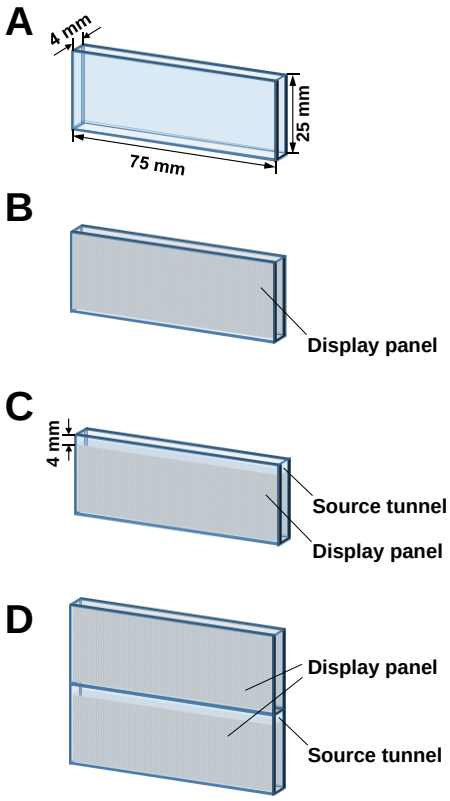

fig. S6. Preparation of the thin scattering plate assembly containing a source tunnel flanked by two display panels. (**A**) An empty thin display panel made by microscope cover slides with dimensions of 75 mm × 25 mm × 4 mm. (**B**) Illustration of the top display panel. (**C**) Illustration of the bottom display panel with a source tunnel. (**D**) Illustration of the completed plate assembly.

Supplementary movie captions

movie S1. Simulated instantaneous light-scattering pattern in a thin scattering sheet under superluminal conditions (M_p = 1.4).

movie S2. Simulated instantaneous light-scattering pattern in a thin scattering sheet under subluminal conditions (M_p = 0.8).

movie S3. Animated illustration of the LLE-CUP system.

movie S4. Experimentally imaged laser pulse propagation under superluminal conditions (M_p = 1.4) through a thin scattering plate assembly that contains air (refractive index n_s = 1.0) as the source tunnel medium and silicone rubber (refractive index n_d = 1.4) mixed with scattering aluminum oxide powder as the medium of the display panels.

movie S5. Experimentally imaged laser pulse propagation under subluminal conditions (M_p = 0.8) through a thin scattering plate assembly that contains liquid oil with a high refractive index (refractive index n_s = 1.8) as the source tunnel medium and silicone rubber (refractive index n_d = 1.4) mixed with scattering aluminum oxide powder as the medium of the display panels.

movie S6. Comparative image reconstructions of a superluminal light wavefront sweeping across a car-model target using first-generation CUP and LLE-CUP.